Research Article

Amal Al-Hanaya and Shreen El-Sapa*

Impact of permeability and fluid parameters in couple stress media on rotating eccentric spheres

https://doi.org/10.1515/phys-2024-0112
received September 30, 2024; accepted December 25, 2024

Abstract: This study elucidates the axisymmetric rotation of two eccentric spheres immersed in an incompressible couple stress fluid within a porous annular region. The investigation incorporates boundary conditions applied to the surfaces of both spheres, which rotate axially at differing angular velocities. Utilizing a collocation scheme alongside a semi-analytical approach under the assumption of low Reynolds numbers, this research delves into the hydrodynamic couple force (torque) exerted by the Brinkman couple stress fluid on the interior sphere. The analysis reveals that the dimensionless torque becomes increasingly significant as permeability enhances the size ratio, couple stress fluid parameters, and separation distance. The computed torque values due to stress and couple stress are presented graphically, providing visual clarity to the findings. Additionally, all the results align closely with the numerical analysis of two eccentric rigid spheres in conventional couple stress fluids, devoid of permeability effects or slip conditions, as demonstrated in previous studies (Al-Hanaya and El-Sapa (Effects of slippage and permeability of couple stress fluid squeezed between two concentric rotating spheres. Phys Fluids. 2023;35:103112); Al-Hanaya *et al.* (Axisymmetric motion of an incompressible couple stress fluid between two eccentric rotating spheres. J Appl Mech Tech Phys. 2022;63(5):1–9)).

Keywords: numerical method, interaction: couple stress fluid, permeability, torque

Nomenclature

(r, θ, ϕ)	spherical polar coordinates
$\vec{q}$	velocity vector of fluid (m/s)
U	characteristic velocity
ξ	couple stress parameter $\sqrt{a^2\mu/\eta}$
α	permeability parameter $\sqrt{a^2/K}$
μ, λ	viscosity coefficient (Pa s)
η, η'	couple stress viscosity coefficients (Pa s)
ρ	density of the fluid (kg/m^3)
$\vec{\omega}$	spin vector
f	body force per unit mass (m/s^2)
c	body couple per unit mass (m^2/s^2)
M	couple stress diadic
p	pressure (Pa (N/m^2))
E	rate of deformation tensor
m	trace of couple stress tensor
Ω	characteristic angular velocity (1/s)

1 Introduction

For the past 50 years, researchers have concentrated on understanding fluid flow through porous materials. Numerous applications, including heat exchange, separation, filtration, increased soil contamination, shale gas extraction, oil recovery, and catalytic assistance in industry, require an understanding of flow behavior in porous media. Fluid flow in a porous material that is isotropic and homogenous on a large scale is governed by either Darcy's law or Brinkman's equations. Porosity has a negligible impact on Darcy's law. However, because Darcy's law cannot resolve an issue with high porosity and a high tangential rate, one runs into difficulties. This problem is solved by applying Brinkman's equation [1]. Leontev [2] studied the Newtonian fluid flow past spheres and cylinders in a porous media under Navier boundary conditions. El-Sapa [3] proposed an analytical method for thermophoresis of particles in the center of a spherical cavity that was filled with Brinkman's porous medium. The mobility of a spherical particle was investigated by Faltas *et al.* in the context

*** Corresponding author: Shreen El-Sapa,** Department of Mathematical Sciences, College of Science, Princess Nourah bint Abdulrahman University, P.O. Box 84428, Riyadh 11671, Saudi Arabia,
e-mail: seelsapa@pnu.edu.sa
Amal Al-Hanaya: Department of Mathematical Sciences, College of Science, Princess Nourah bint Abdulrahman University, P.O. Box 84428, Riyadh 11671, Saudi Arabia

of a semi-infinite Brinkman flow [4]. Madasu and Bucha [5] studied magnetohydrodynamics' effect on micropolar fluid flow around a sphere in Brinkman's porous medium.

Couple stress fluids are useful in real life. Bio-fluids, colloidal fluids, liquid crystals, and others are couple stress fluids. Polar effects in couple stress fluid flow were initially studied by Stokes [6]. Stokes [7] proposed a basic theory to explain fluid polar phenomena and generalize classical theory. Stokes discovered that the polar effect in fluids is a result of couple stresses and body couplings. He also observed that the mechanical action is analogous to both forces and momentum distributions. Couple stresses lead to a size-dependent effect that is not accounted for in classical hydrodynamics. However, it is essential in specific cases, such as fluid flows with suspended particles, colloidal fluids, or liquid crystals. Many studies have examined the utilization of these fluids. Jangili *et al.* [8] examined how thermal conductivity and viscosity affect couple stress fluid flow irreversibility between asymmetrically heated parallel plates. Al-Hanaya *et al.* [9] researched the axisymmetric movement of fluid couple stress between two eccentric spinning spheres. They found that the solid sphere's normalized torque rotates inside the outer sphere without slipping. The normalized torque rises with the size ratio and separation distance. Couple stress fluids have been utilized in many porous media, such as in the studies conducted by El-Sapa and Almoneef [10], focusing on the axisymmetric flow of aerosol particles under a slippage regime.

Many natural applications exist for the flow motion theory of two eccentric spheres in micropolar fluids and rheological fluids. Fluid microstructure can affect limited and asymmetric flow inflow performance. Majumdar investigated the asymmetrical homogenous incompressible viscous liquid flow in the annulus between two rigid spheres [11]. Kamel *et al.* [12] studied micropolar liquid flow around two rolling rigid spheres. Munson [13] studied eccentric Newtonian fluid flow. Recently, Sherief *et al.* [14] used semi-analytical methods to solve the no-slip problem of pushing a sphere into a non-concentric spherical hollow that was filled with creeping micropolar fluid. El-Sapa [15] examined the relationship between a spherical envelope with a slip regime and a non-concentric rigid sphere submerged in a micropolar fluid. Al-Hanaya *et al.* [9] considered a slow, steady motion of a couple stress fluid between two non-concentric, rotating spherical boundaries.

The torque generated by the rotation of solid particles in incompressible Newtonian, non-Newtonian, or porous media has applications in the domains of chemistry, biomedicine, environmental science, and other scientific disciplines. Scientists have analyzed the occurrence of torque in the movement of spheres, cylinders, and other geometric shapes in a couple of stress fluids. Davis [16] studied the force and torque on a rotating sphere close to and within a fluid-filled rotating sphere. Madasu and Sarkar [17] conducted an assessment of the torque exerted on the slow rotation of a slightly deformed slip sphere in a Brinkman medium. In the context of the Theory of Porous Media, this work introduces a two-scale Mesh-in-Element (MIEL) approach that allows for finite element discretization and significant scale coupling. It investigates the theoretical underpinnings, algorithmic implementation, and application of MIEL for modeling heterogeneous, inelastic materials, building on prior research and verifying its efficacy using numerical examples by Maike *et al.* [18]. Also, El-Sapa and Al-Hanaya [19] examined how variations in slip conditions at the fluid interfaces and the permeability of the medium affect the flow characteristics by employing mathematical modeling and analytical techniques in two concentric spheres with couple stress fluid in the annulus. Further studies [20,21] explore fluid dynamics within annular geometries, focusing on peristaltic motion and magnetohydrodynamic effects. Their initial study formulates a mathematical model for blood flow in a porous annular space between deformable tubes, providing valuable insights for peristaltic endoscopes. Then, they develop a mathematical model for creeping electro-magnetohydrodynamic peristaltic propulsion in an annular gap created by sinusoidally deforming tubes. Together, these studies contribute to a deeper theoretical understanding of fluid dynamics in both medical and engineering applications.

According to the aforementioned literature review, this study looks into the Brinkman couple stress fluid between two spinning eccentric spheres, which has many potential applications, such as tribology, which is understanding the lubrication behavior of non-Newtonian fluids in eccentric geometries; also biomechanics such as modeling the flow of blood or other biological fluids in vessels with irregular shapes; and finally, chemical engineering, such as analyzing the mixing and transport of non-Newtonian fluids in industrial processes. The solutions are obtained with analytical and numerical approaches, and there are other numerical methods, such as finite element or finite difference methods, that can be employed to solve the governing equations.

2 Field equations and constitutive relations

In 1984, Stokes [6] extended the well-known Navier–Stokes theory to develop the micro-continuum theory of couple

stress fluid. The Stokes theory takes into account the impact of particle size as well as the presence of polar effects in the fluid medium, such as couple stress, body couple stress, and asymmetric stress. Previous studies [18,19] provide the revised equations, which regulate the continuity and momentum of an incompressible fluid with couple stress in Brinkman's medium as

$$\nabla\cdot\vec{q} = 0, \tag{2.1}$$

$$\nabla p + \mu\nabla\wedge\nabla\wedge\vec{q} + \eta\nabla\wedge\nabla\wedge\nabla\wedge\nabla\wedge\vec{q} + \frac{\mu}{K}\vec{q} = 0, \tag{2.2}$$

where $\vec{q}$ is the volume-averaged velocity, p is the pore average pressure, μ represents the viscosity of the fluid, η is the first couple stress viscosity coefficient, and η' is the second couple stress viscosity coefficient. If the couple stress coefficient η is taken to be zero, then the equation of motion (2.2) reduces to the classical Navier–Stokes's equation. The fluid velocity *via* a porous medium is governed by the following Darcy–Brinkman equation, but we assume that μ_e is the effective viscosity when the fluid flow takes place in the porous medium, which is equal to μ that is suggested by Ochoa-Tapia and Whitaker [24,25]. In addition, K is the Darcy permeability of the permeable medium and also is a scalar for isotropic porous medium. Otherwise, K is a second-order tensor [26] and the Brinkman equation of couple stress fluid reduces to the Darcy equation when $K\to 0$ and to the Stokes equation of couple stress fluid when $K\to\infty$.

The constitutive equations of the stress dyadic Π and couple stress dyadic M of the couple stress fluids are given by [7,9]

$$\Pi = -pI + \lambda\nabla\cdot\vec{q} + 2\mu E + \frac{1}{2}I\wedge\nabla\cdot M, \tag{2.3}$$

$$M = mI + 4\eta\nabla\vec{\omega} + 4\eta'(\nabla\vec{\omega})^T, \tag{2.4}$$

where $E = \frac{1}{2}(\nabla\vec{q} + (\nabla\vec{q})^T)$ is the deformation dyadic, I is the unit dyadic, and $\vec{\omega}$ is the vorticity vector. Here, $(\cdot)^T$ denotes the transpose of a dyadic. The viscosity coefficients in couple stress fluid equations satisfy these inequalities:

$$\mu \geq 0, \eta \geq 0, \eta \geq \eta', 3\lambda + 2\mu \geq 0. \tag{2.5}$$

Introducing the dimensionless quantities to the governing Eq. (2.2), we obtain the following:

$$\begin{aligned} &\vec{q}' = \frac{\vec{q}}{a\Omega}, \quad \vec{\omega}' = \frac{\vec{\omega}}{\Omega}, \quad p' = \frac{p}{\mu\Omega},\\ &\nabla' = a\nabla, \quad \hat{\tau}_{rr} = \frac{\tau_{rr}}{\mu\Omega}, \quad \alpha^2 = \frac{a^2}{K},\\ &\xi^2 = \frac{a^2\mu}{\eta}, \quad r' = \frac{r}{a}, \quad m' = \frac{am}{\mu\Omega}. \end{aligned} \tag{2.6}$$

Substituting Eq. (2.8) in Eq. (2.7) and then dropping the primes, we obtain

$$\nabla p + \nabla\wedge\nabla\wedge\vec{q} + \frac{1}{\xi^2}\nabla\wedge\nabla\wedge\nabla\wedge\nabla\wedge\vec{q} + \alpha^2\vec{q} = 0, \tag{2.7}$$

where α is the permeability parameter, and ξ is the length-dependent parameter of the first couple stress fluid coefficient. If $\xi\to\infty = (\eta = 0)$, Eq. (2.7) denotes the improved Stokes equation for non-polar fluids.

Furthermore, the relations of non-dimensional stress and couple stress are obtained by

$$\begin{aligned} \tau_{r\phi} = \frac{\partial q_\phi}{\partial r} - \frac{q_\phi}{r} + \frac{1}{2}\Bigg[\frac{\partial m_{r\theta}}{\partial r} + \frac{1}{r}(2m_{r\theta} + m_{\theta r})\\ + \frac{\cot\theta}{r}(m_{\theta\theta} - m_{\phi\phi}) + \frac{1}{r}\frac{\partial m_{\theta\theta}}{\partial\theta}\Bigg], \end{aligned} \tag{2.8}$$

where

$$m_{rr} = \bar{m} + 4\left(\frac{1}{\xi^2} + \frac{1}{\xi'^2}\right)\frac{\partial\omega_r}{\partial r}, \tag{2.9}$$

$$m_{r\theta} = \frac{4}{\xi^2}\frac{\partial\omega_\theta}{\partial r} + \frac{4}{\xi'^2}\frac{1}{r}\left(\frac{\partial\omega_r}{\partial\theta} - \omega_\theta\right), \tag{2.10}$$

$$m_{\theta\theta} = \bar{m} + 4\frac{1}{r}\left(\frac{1}{\xi^2} + \frac{1}{\xi'^2}\right)\left(\frac{\partial\omega_\theta}{\partial\theta} + \omega_r\right), \tag{2.11}$$

$$m_{\theta r} = \frac{4}{\xi^2}\frac{1}{r}\left(\frac{\partial\omega_r}{\partial\theta} - \omega_\theta\right) + \frac{4}{\xi'^2}\frac{\partial\omega_\theta}{\partial r}, \tag{2.12}$$

$$m_{\phi\phi} = \bar{m} + 4\frac{1}{r}\left(\frac{1}{\xi^2} + \frac{1}{\xi'^2}\right)(\omega_r + \cot\theta\omega_\theta), \tag{2.13}$$

where $\xi'^2 = \frac{a^2\mu}{\eta'}$ is the length-dependent parameter on the second couple stress fluid coefficient.

3 Axisymmetric solutions to the problem

Suppose a solid sphere rotates through unbounded Brinkman couple stress fluids. Therefore, the origin of the spherical coordinate system (r, θ, ϕ) is positioned in the center of the sphere. The flow field functions are independent of ϕ due to symmetry. Additionally, the vectors of velocity and vorticity have the form:

$$\vec{q} = q_\phi(r,\theta)\vec{e}_\phi, \quad \vec{\omega} = \omega_r\vec{e}_r + \omega_\theta\vec{e}_\theta, \tag{3.1}$$

where $\vec{e}_r$, $\vec{e}_\theta$, and $\vec{e}_\phi$ are the unit vectors along the coordinate lines r, θ, and ϕ. Applying Eq. (3.1) into (2.7), we obtain the fourth-order partial differential equation as follows:

$$(L_{-1} - \lambda_1^2)(L_{-1} - \lambda_2^2)(r\sin\theta q_\phi) = 0, \tag{3.2}$$

where the axisymmetric Stokesian differential operator L_{-1} and the roots are expressed as

$$\left.\begin{aligned} L_{-1} &= \frac{\partial^2}{\partial r^2} + \frac{1-\zeta^2}{r^2}\frac{\partial^2}{\partial \xi^2}, \quad \zeta = \cos\theta, \\ \lambda_1^2 + \lambda_2^2 &= \xi^2, \lambda_1^2\lambda_2^2 = \xi^2\alpha^2 \\ \lambda_{ij} &= \pm\sqrt{\frac{\xi^2 \pm \xi\sqrt{\xi^2 - 4\alpha^2}}{2}}, \quad i,j = 1,2 \end{aligned}\right\}. \tag{3.3}$$

The non-zero vorticity components ω_r and ω_θ are expressed as

$$\left.\begin{aligned} \vec{\omega}_r &= \frac{1}{2}(\nabla \wedge \vec{q})\cdot \vec{e}_r = \frac{1}{2}\frac{1}{r\sin\theta}\frac{\partial}{\partial\theta}(\sin\theta q_\phi), \\ \vec{\omega}_\theta &= \frac{1}{2}(\nabla \wedge \vec{q})\cdot \vec{e}_\theta = -\frac{1}{2}\frac{1}{r}\frac{\partial}{\partial r}(rq_\phi). \end{aligned}\right\} \tag{3.4}$$

On the rotating solid sphere, the following boundary conditions have two possible situations that were made assumptions by Stokes [9]: boundary conditions (A) declare that there are no couple stresses at the border of the region and (B) the second states that the angular velocity of the boundary is equivalent to the vorticity along the boundary. Physically, according to the first boundary condition, the tangential velocity at the sphere's surface depends on the polar angle θ and is proportionate to the angular velocity. This condition emphasizes that there is no surface slip for the tangential component of the velocity and illustrates how the fluid or surface interacts with the rotating sphere. The second boundary condition indicates that the sphere is not under any extra couple stresses. This indicates that there are no moments created by the applied forces that would result in rotation around an axis. By demonstrating that the stresses are entirely normal or shear with no twisting effects, this condition streamlines the analysis:

(1) The no-slip condition:

$$q_\phi = a\Omega\sin\theta, \tag{3.5}$$

(2) No couple stresses (Type A):

$$m_{ij}n_i = 0, \tag{3.6}$$

where Ω is the characteristic angular velocity, and the range of the slip coefficient, β, is zero to infinity. Only the kind of fluid flow and the boundary's substance affect this parameter. From this study, the perfect slipcase may be reached when the slip coefficient disappears, and the classical situation of no slip can be inferred as a special case when the slip parameter approaches infinity. In addition, n is the unit normal to the solid sphere's surface. The aforementioned boundary conditioning was proposed by Stokes [6]. According to physical theory, a force distribution can only result from mechanical interactions at the boundaries in this particular situation.

Consequently, the differential Eq. (3.2) has the following generic solution:

$$\begin{aligned} q_\phi(r,\theta) = \sum_{j=1}^{2}\sum_{n=1}^{\infty}\Big[&A_n^{(j)}r^{-\frac{1}{2}}K_{n+\frac{1}{2}}(\lambda_{1j}r) \\ &+ B_n^{(j)}r^{-\frac{1}{2}}I_{n+\frac{1}{2}}(\lambda_{2j}r)\Big]P_n^1(\cos\theta), \end{aligned} \tag{3.7}$$

where the functions $K_n(\cdot)$ and $I_n(\cdot)$ are the modified Bessel functions of the first and second kinds of order n, respectively. where $A_n^{(j)}, B_n^{(j)}, j = 1, 2$ are the constants. Also, $P_n^1(\cdot)$ represents the associated Legendre polynomials of degree n and order one. The components of vorticity are obtained by

$$\begin{aligned} \omega_r(r,\theta) = \frac{1}{2}\sum_{j=1}^{2}\sum_{n=1}^{\infty} &n(n+1)r^{-\frac{3}{2}}P_n(\cos\theta) \\ &\times\Big[A_n^{(j)}K_{n+\frac{1}{2}}(\lambda_{1j}r) + B_n^{(j)}I_{n+\frac{1}{2}}(\lambda_{2j}r)\Big], \end{aligned} \tag{3.8}$$

$$\begin{aligned} \omega_\theta(r,\theta) = \frac{1}{2}\sum_{j=1}^{2}\sum_{n=1}^{\infty} &r^{-\frac{3}{2}}P_n^1(\cos\theta) \\ &\times\Big[A_n^{(j)}\Big(nK_{n+\frac{1}{2}}(\lambda_{1j}r) + \lambda_{1j}rK_{n-\frac{1}{2}}(\lambda_{1j}r)\Big) \\ &+ B_n^{(j)}\Big(nI_{n+\frac{1}{2}}(\lambda_{2j}r) - \lambda_{2j}rI_{n-\frac{1}{2}}(\lambda_{2j}r)\Big)\Big]. \end{aligned} \tag{3.9}$$

Furthermore, the couple stress functions are obtained from (2.9)–(2.13) as follows:

$$\begin{aligned} m_{r\theta}(r,\theta) = 2\sum_{j=1}^{2}\sum_{n=1}^{\infty} &r^{-\frac{5}{2}}P_n^1(\cos\theta) \\ &\times\Big[-A_n^{(j)}\Big((\xi^{-2} + \xi'^{-2})\lambda_{1j}rK_{n-\frac{1}{2}}(\lambda_{1j}r) \\ &+ (\xi^{-2}\lambda_{1j}^2r^2 + (\xi^{-2} + \xi'^{-2})n(n \\ &+ 2))K_{n+\frac{1}{2}}(\lambda_{1j}r)\Big) + B_n^{(j)}((\xi^{-2} + \xi'^{-2}) \\ &\times\lambda_{2j}rI_{n-\frac{1}{2}}(\lambda_{2j}r) - (\xi^{-2}\lambda_{2j}^2r^2 \\ &+ (\xi^{-2} + \xi'^{-2})n(n+2))I_{n+\frac{1}{2}}(\lambda_{2j}r)\Big)\Big], \end{aligned} \tag{3.10}$$

$$
\begin{aligned}
m_{\theta r}(r,\theta) = 2\sum_{j=1}^{2}\sum_{n=1}^{\infty} r^{-\frac{5}{2}}P_n^1(\cos\theta)\\
\times\Bigg[-A_n^{(j)}\Bigg((\xi^{-2}+\xi'^{-2})\lambda_{1j}rK_{n-\frac{1}{2}}(\lambda_{1j}r)\\
+(\xi'^{-2}\lambda_{1j}^2r^2+(\xi^{-2}+\xi'^{-2})n(n\\
+2))K_{n+\frac{1}{2}}(\lambda_{1j}r)\Bigg)+B_n^{(j)}((\xi^{-2}+\xi'^{-2})\\
\times\lambda_{2j}rI_{n-\frac{1}{2}}(\lambda_{2j}r)-(\xi'^{-2}\lambda_{2j}^2r^2\\
+(\xi^{-2}+\xi'^{-2})n(n+2))I_{n+\frac{1}{2}}(\lambda_{2j}r)\Bigg)\Bigg],
\end{aligned}
\tag{3.11}
$$

$$
\begin{aligned}
m_{\theta\theta}(r,\theta) = m+2(\xi^{-2}+\xi'^{-2})\sum_{j=1}^{2}\sum_{n=1}^{\infty}(n+1)r^{-\frac{5}{2}}P_n(\cos\theta)\\
\times[-A_n^{(j)}\Bigg(\csc\theta\lambda_{1j}rK_{n-\frac{1}{2}}(\lambda_{1j}r)\\
+n(\csc\theta-1)K_{n+\frac{1}{2}}(\lambda_{1j}r)\Bigg)\\
+B_n^{(j)}\Bigg(\csc\theta\lambda_{2j}rI_{n-\frac{1}{2}}(\lambda_{2j}r)-n(\csc\theta-1)\\
I_{n+\frac{1}{2}}(\lambda_{2j}r)\Bigg)\Bigg]+r^{-\frac{5}{2}}\cot\theta P_n^1(\cos\theta)\\
\times\Bigg[A_n^{(j)}\Bigg(\lambda_{1j}rK_{n-\frac{1}{2}}(\lambda_{1j}r)+nK_{n+\frac{1}{2}}(\lambda_{1j}r)\Bigg)\\
-B_n^{(j)}\Bigg(\lambda_{2j}rI_{n-\frac{1}{2}}(\lambda_{2j}r)-nI_{n+\frac{1}{2}}(\lambda_{2j}r)\Bigg)\Bigg],
\end{aligned}
\tag{3.12}
$$

$$
\begin{aligned}
m_{\phi\phi}(r,\theta) = m+2(\xi^{-2}+\xi'^{-2})r^{-\frac{5}{2}}\sum_{j=1}^{2}\sum_{n=1}^{\infty}n(n\\
+1)P_n(\cos\theta)\\
\times\Bigg[A_n^{(j)}K_{n+\frac{1}{2}}(\lambda_{1j}r)+B_n^{(j)}I_{n+\frac{1}{2}}(\lambda_{2j}r)\Bigg]\\
+\cot\theta P_n^1(\cos\theta)\Bigg[A_n^{(j)}\Bigg(\lambda_{1j}rK_{n-\frac{1}{2}}(\lambda_{1j}r)\\
+nK_{n+\frac{1}{2}}(\lambda_{1j}r)\Bigg)-B_n^{(j)}\Bigg(\lambda_{2j}rI_{n-\frac{1}{2}}(\lambda_{2j}r)\\
-nI_{n+\frac{1}{2}}(\lambda_{2j}r)\Bigg)\Bigg].
\end{aligned}
\tag{3.13}
$$

Hence, from Eq. (3.6), we obtain $m_{rr} = 0$ on the surface of the object.

$$
\begin{aligned}
m_{rr}(r,\theta) = 2(\xi^{-2}+\xi'^{-2})\sum_{j=1}^{2}\sum_{n=1}^{\infty}r^{-\frac{3}{2}}n(n+1)P_n^1(\cos\theta)\\
\times\Bigg[A_n^{(j)}\Bigg(\lambda_{1j}rK_{n-\frac{1}{2}}(\lambda_{1j}r)+(n+2)K_{n+\frac{1}{2}}(\lambda_{1j}r)\Bigg)\\
-B_n^{(j)}\Bigg(\lambda_{2j}rI_{n-\frac{1}{2}}(\lambda_{2j}r)-(n+2)I_{n+\frac{1}{2}}(\lambda_{2j}r)\Bigg)\Bigg].
\end{aligned}
\tag{3.14}
$$

Inserting Eqs (3.7) and (3.10)–(3.14) into (2.8), we obtain

$$
\begin{aligned}
\tau_{r\phi}(r,\theta) = r^{-\frac{7}{2}}\sum_{j=1}^{2}\sum_{n=1}^{\infty}2\sigma\cos\theta\csc^2\theta P_n(\cos\theta)\\
\times\Bigg[-A_n^{(j)}\Bigg(\lambda_{1j}rK_{n-\frac{1}{2}}(\lambda_{1j}r)+nK_{n+\frac{1}{2}}(\lambda_{1j}r)\Bigg)\\
+B_n^{(j)}\Bigg(\lambda_{2j}rI_{n-\frac{1}{2}}(\lambda_{2j}r)-nI_{n+\frac{1}{2}}(\lambda_{2j}r)\Bigg)\Bigg]\\
+\csc^2\theta P_n^1(\cos\theta)[A_n^{(j)}((-\cos^2\theta(\sigma_1+\sigma\csc\theta)\\
+\sigma_3+\sigma\csc\theta)\lambda_{1j}rK_{n-\frac{1}{2}}(\lambda_{1j}r)\\
+(-\cos^2\theta(\sigma_7+n\sigma\csc\theta)\\
+\sigma_5+n\sigma\csc\theta)K_{n+\frac{1}{2}}(\lambda_{1j}r)\Bigg)\\
+B_n^{(j)}\Bigg((\cos\theta^2(\sigma_2+\sigma\csc\theta)-\sigma_4\\
-\sigma\csc\theta)\lambda_{2j}rI_{n-\frac{1}{2}}(\lambda_{2j}r)\\
+(-\cos^2\theta(\sigma_8+n\sigma\csc\theta)+\sigma_6\\
+n\sigma\csc\theta)I_{n+\frac{1}{2}}(\lambda_{2j}r)\Bigg)\Bigg],
\end{aligned}
\tag{3.15}
$$

where

$$
\begin{aligned}
\sigma &= (n+1)(\xi^{-2}+\xi'^{-2}),\\
\sigma_1 &= \lambda_{1j}^2r^2\xi^{-2}-r^2-2\xi^{-2}-2\xi'^{-2},\\
\sigma_2 &= \lambda_{2j}^2r^2\xi^{-2}-r^2-2\xi^{-2}-2\xi'^{-2},\\
\sigma_3 &= \lambda_{1j}^2r^2\xi^{-2}-r^2-\xi^{-2}-\xi'^{-2},\\
\sigma_4 &= \lambda_{2j}^2r^2\xi^{-2}-r^2-\xi^{-2}-\xi'^{-2},\\
\sigma_5 &= \lambda_{1j}^2r^2\xi^{-2}n-(n+2)r^2-n(2n+3)(\xi^{-2}+\xi'^{-2}),\\
\sigma_6 &= \lambda_{2j}^2r^2\xi^{-2}n-(n+2)r^2-n(2n+3)(\xi^{-2}+\xi'^{-2}),\\
\sigma_7 &= \lambda_{1j}^2r^2\xi^{-2}n-(n+2)r^2-2n\sigma,\\
\sigma_8 &= \lambda_{2j}^2r^2\xi^{-2}n-(n+2)r^2-2n\sigma.
\end{aligned}
$$

4 Torque due to stress and couple stress tensors

Torque in fluids arises from the forces due to stress and, in couple stress fluids, additional microstructural effects. In classical fluids, torque results from pressure and viscous forces acting on surfaces, calculated using the stress tensor. In couple stress fluids, which account for internal body and surface couples, torque includes contributions from both the stress tensor and the couple stress tensor, reflecting the fluid's microstructure. These effects are significant in systems such as suspensions, polymer solutions, and microfluidic devices, influencing rotational dynamics, lubrication, and energy dissipation. This enhances the fluid's ability to model behaviors in complex systems.

The torque $T_z\vec{e}_z$ of the fluid flow affecting the axisymmetric particle is controlled on the solid of revolution and calculated according to the following [27]:

$$T_z = 2\pi\mu a^3 \int_0^{\pi} \tau_{r\phi}\,|_{r=a} \sin^2\theta \mathrm{d}\theta. \tag{4.1}$$

Substituting Eq. (3.15) into formula (4.1), we obtain

$$\begin{aligned} T_z = {} & 2\pi\mu a^{-\frac{1}{2}} \sum_{j=1}^{2} \pi\Big[-A_1^{(j)}\Big(\lambda_{1j} a K_{\frac{1}{2}}(\lambda_{1j}a) + K_{\frac{3}{2}}(\lambda_{1j}a)\Big) \\ & + B_1^{(j)}\Big(\lambda_{2j} a I_{\frac{1}{2}}(\lambda_{2j}a) - I_{\frac{3}{2}}(\lambda_{2j}a)\Big)\Big] \\ & + I\Big[A_1^{(j)}\Big(\Big(-\frac{2}{3}\sigma_1 + \frac{1\pi}{2}\sigma + 2\sigma_3\Big)\lambda_{1j} a K_{\frac{1}{2}}(\lambda_{1j}a) \\ & + \Big(-\frac{2}{3}\sigma_7 + \frac{1\pi}{2}\sigma + 2\sigma_5\Big)K_{\frac{3}{2}}(\lambda_{1j}a)\Big) \\ & + B_1^{(j)}\Big(\Big(\frac{2}{3}\sigma_2 - \frac{\pi}{2}\sigma - 2\sigma_4\Big)\lambda_{2j} a I_{\frac{1}{2}}(\lambda_{2j}a) \\ & + \Big(-\frac{2}{3}\sigma_8 + \frac{\pi}{2}\sigma + 2\sigma_6\Big)I_{\frac{3}{2}}(\lambda_{2j}a)\Big)\Big]. \end{aligned} \tag{4.2}$$

The torque T_m due to the couple stress tensor exerted on a spherical particle, a_1 is

$$T_m = 2\pi\mu a^2 \int_0^{\pi} (m_{rr}\cos\theta - m_{r\theta}\sin\theta)|_{r=a} \sin\theta d\theta. \tag{4.3}$$

Substituting (3.10) and (3.14) into (4.3), we obtain

$$\begin{aligned} T_m = {} & -2I\pi^2\mu a^{-\frac{1}{2}} \sum_{j=1}^{2} \times \Big[-A_1^{(j)}\Big((\xi^{-2} + \xi'^{-2})\lambda_{1j} a K_{\frac{1}{2}}(\lambda_{1j}a) \\ & + (\xi^{-2}\lambda_{1j}^2 a^2 + (\xi^{-2} + 3\xi'^{-2}))K_{\frac{3}{2}}(\lambda_{1j}a)\Big) \\ & + B_1^{(j)}\Big((\xi^{-2} + \xi'^{-2})\lambda_{2j} a I_{\frac{1}{2}}(\lambda_{2j}a) \\ & - (\xi^{-2}\lambda_{2j}^2 a^2 + (\xi^{-2} + \xi'^{-2})n(n+2))I_{\frac{3}{2}}(\lambda_{2j}a)\Big)\Big]. \end{aligned} \tag{4.4}$$

5 Interaction between two eccentric spheres

We examine the steady couple stress incompressible fluid flow produced by two rotating eccentric spheres of radii a_1 and a_2 with two angular velocities Ω_1 and Ω_2, respectively, around their common diameter (z-axis), as illustrated in Figure 1. The spherical coordinates, in this case, are (r_2, θ_2, ϕ_2) with the origin at the outside sphere center and (r_1, θ_1, ϕ_1) based on the inside solid sphere center, which is situated at a distance of h from the cavity center. Suppose that couple stress fluids rotate consistently in an axisymmetric direction around a sphere of radius a_1. The flow field functions are invariant with respect to ϕ due to symmetry. Furthermore, the velocity and vorticity vectors are expressed as

$$\vec{q} = q_\phi(r,\theta)\vec{e}_\phi \quad \text{and} \quad \vec{\omega} = \omega_r\vec{e}_r + \omega_\theta\vec{e}_\theta, \tag{5.1}$$

where $\vec{e}_r$, $\vec{e}_\theta$, and $\vec{e}_\phi$ represent the unit vectors along the coordinate lines r, θ, and ϕ. Furthermore, the coordinate systems (r_1, θ_1, ϕ_1) and (r_2, θ_2, ϕ_2) are connected by the following relations (r_1, θ_1) and (r_2, θ_2) is given by $r_1^2 = r_2^2 + h^2 - 2r_2h\cos\theta_2$ or by $r_2^2 = r_1^2 + h^2 + 2r_1h\cos\theta_1$. The equations' linearity enables the application of the superposition principle. However, we choose the velocity $\vec{q}_\phi^{(j)}$ and the tangential couple stress functions $m_{r\theta}^{(j)}$ in the form:

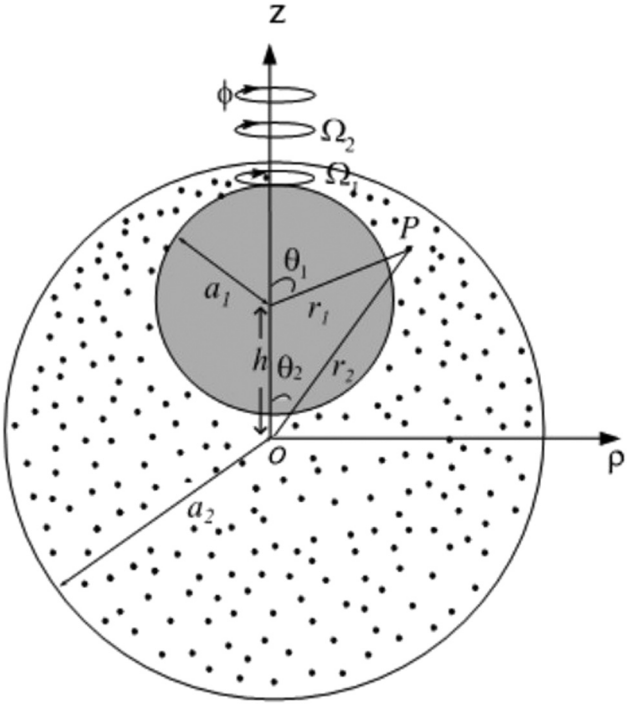

Figure 1: Sketch of Brinkman couple stress fluid between two rotating eccentric spheres.

$$\left.\begin{aligned}\vec{q}_{\phi}^{(j)}(r_j,\theta_j) &= q_{\phi}^{(1)}(r_1,\theta_1) + q_{\phi}^{(2)}(r_2,\theta_2),\\ m_{r_j\theta_j}^{(j)}(r_j,\theta_j) &= m_{r_1\theta_1}^{(1)}(r_1,\theta_1) + m_{r_2\theta_2}^{(2)}(r_2,\theta_2).\end{aligned}\right\} \tag{5.2}$$

From the differential Eq. (3.2), four boundary conditions are required to describe the problem. The boundary conditions on the surfaces of the spheres are established as follows:

$$r_1 = a_1: \quad q_{\phi} = a_1\Omega_1\sin\theta_1, \quad m_{r_1\theta_1} = 0, \tag{5.3}$$

$$r_2 = a_2: \quad q_{\phi} = a_2\Omega_2\sin\theta_2, \quad m_{r_2\theta_2} = 0, \tag{5.4}$$

where Ω_j, $j = 1, 2$ are the angular velocities of the two spheres. Accordingly, the mechanical interaction at the wall is equivalent to the no-slip condition at the boundary, which states that all solid borders have zero fluid velocity. In addition, boundary walls can prevent fluid elements from rotating, so there is no zero couple stress when it comes to boundary walls. The field functions, the velocity, and the couple stress are given by

$$\begin{aligned}q_{\phi}(r,\theta) = &\sum_{j=1}^{2}\sum_{n=1}^{\infty} A_n^{(j)} r_1^{-\frac{1}{2}} K_{n+\frac{1}{2}}(\lambda_{1j}r_1) P_n^1(\cos\theta_1)\\ &+ \sum_{j=1}^{2}\sum_{n=1}^{\infty} B_n^{(j)} r_2^{-\frac{1}{2}} I_{n+\frac{1}{2}}(\lambda_{2j}r_2) P_n^1(\cos\theta_2),\end{aligned} \tag{5.5}$$

$$\begin{aligned}m_{\theta r}(r,\theta) = &-2\sum_{j=1}^{2}\sum_{n=1}^{\infty} r_1^{-\frac{5}{2}} P_n^1(\cos\theta_1) A_n^{(j)}\\ &\times\Big((\xi^{-2}+\xi'^{-2})\lambda_{1j}r_1 K_{n-\frac{1}{2}}(\lambda_{1j}r_1)\\ &+ (\xi'^{-2}\lambda_{1j}^2 r_1^2 + (\xi^{-2}+\xi'^{-2})n(n\\ &+2))K_{n+\frac{1}{2}}(\lambda_{1j}r_1)\Big)\\ &+ 2\sum_{j=1}^{2}\sum_{n=1}^{\infty} r_2^{-\frac{5}{2}} P_n^1(\cos\theta_2) B_n^{(j)}\\ &\Big((\xi^{-2}+\xi'^{-2})\lambda_{2j}r_2 I_{n-\frac{1}{2}}(\lambda_{2j}r_2)\\ &- (\xi'^{-2}\lambda_{2j}^2 r_2^2 + (\xi^{-2}+\xi'^{-2})n(n+2))I_{n+\frac{1}{2}}(\lambda_{2j}r_2)\Big)\\ &.\end{aligned} \tag{5.6}$$

Substituting the field functions from (5.5) and (5.6) into the boundary conditions from Eqs (5.3) and (5.4), we have the linear system of equations in the four unknowns $A_n^{(j)}, B_n^{(j)}, j = 1, 2$ as

$$\begin{aligned}a_1\Omega_1\sin\theta_1 = &\sum_{j=1}^{2}\sum_{n=1}^{\infty} A_n^{(j)} a_1^{-\frac{1}{2}} K_{n+\frac{1}{2}}(\lambda_{1j}a_1) P_n^1(\cos\theta_1)\\ &+ \sum_{j=1}^{2}\sum_{n=1}^{\infty} B_n^{(j)} r_2^{-\frac{1}{2}} I_{n+\frac{1}{2}}(\lambda_{2j}r_2)\Big|_{r_1=a_1} P_n^1(\cos\theta_2),\end{aligned} \tag{5.7}$$

$$\begin{aligned}a_2\Omega_2\sin\theta_2 = &\sum_{j=1}^{2}\sum_{n=1}^{\infty} A_n^{(j)} r_1^{-\frac{1}{2}} K_{n+\frac{1}{2}}(\lambda_{1j}r_1)\Big|_{r_2=a_2} P_n^1(\cos\theta_1)\\ &+ \sum_{j=1}^{2}\sum_{n=1}^{\infty} B_n^{(j)} a_2^{-\frac{1}{2}} I_{n+\frac{1}{2}}(\lambda_{2j}a_2) P_n^1(\cos\theta_2),\end{aligned} \tag{5.8}$$

$$\begin{aligned}0 = &-2\sum_{j=1}^{2}\sum_{n=1}^{\infty} a_1^{-\frac{5}{2}} P_n^1(\cos\theta_1) A_n^{(j)}\\ &\times\Big((\xi^{-2}+\xi'^{-2})\lambda_{1j}a_1 K_{n-\frac{1}{2}}(\lambda_{1j}a_1)\\ &+ (\xi'^{-2}\lambda_{1j}^2 a_1^2 + (\xi^{-2}+\xi'^{-2})n(n+2))\\ &\times K_{n+\frac{1}{2}}(\lambda_{1j}a_1)\Big) + 2\sum_{j=1}^{2}\sum_{n=1}^{\infty} r_2^{-\frac{5}{2}} P_n^1(\cos\theta_2)\\ &\times B_n^{(j)}\Big((\xi^{-2}+\xi'^{-2})\lambda_{2j}r_2 I_{n-\frac{1}{2}}(\lambda_{2j}r_2)\\ &- (\xi'^{-2}\lambda_{2j}^2 r_2^2 + (\xi^{-2}+\xi'^{-2})n(n+2))I_{n+\frac{1}{2}}(\lambda_{2j}r_2)\Big)\Big|_{r_1=a_1},\end{aligned} \tag{5.9}$$

$$\begin{aligned}0 = &-2\sum_{j=1}^{2}\sum_{n=1}^{\infty} a_1^{-\frac{5}{2}} P_n^1(\cos\theta_1) A_n^{(j)}\\ &\times\Big((\xi^{-2}+\xi'^{-2})\lambda_{1j}a_1 K_{n-\frac{1}{2}}(\lambda_{1j}a_1)\\ &+ (\xi'^{-2}\lambda_{1j}^2 a_1^2 + (\xi^{-2}+\xi'^{-2})n(n+2))K_{n+\frac{1}{2}}(\lambda_{1j}a_1)\Big)\Big|_{r_2=a_2}\\ &+ 2\sum_{j=1}^{2}\sum_{n=1}^{\infty} r_2^{-\frac{5}{2}} P_n^1(\cos\theta_2) B_n^{(j)}\\ &\times\Big((\xi^{-2}+\xi'^{-2})\lambda_{2j}r_2 I_{n-\frac{1}{2}}(\lambda_{2j}r_2)\\ &- (\xi'^{-2}\lambda_{2j}^2 r_2^2 + (\xi^{-2}+\xi'^{-2})n(n+2))I_{n+\frac{1}{2}}(\lambda_{2j}r_2)\Big).\end{aligned} \tag{5.10}$$

Then, from Eqs (4.2) and (4.4), the torque due to stress and couple stress forces T_z and T_m acting on the inside particle $a_1 = 1$ is given by

$$\begin{aligned}T_z = 2\pi\mu a_1^{-\frac{1}{2}}\sum_{j=1}^{2}\pi\times &\Big[-A_1^{(j)}\Big(\lambda_{1j}a_1 K_{\frac{1}{2}}(\lambda_{1j}a_1) + K_{\frac{3}{2}}(\lambda_{1j}a_1)\Big)\\ &+ B_1^{(j)}\Big(\lambda_{2j}a_1 I_{\frac{1}{2}}(\lambda_{2j}a_1) - I_{\frac{3}{2}}(\lambda_{2j}a_1)\Big)\Big]\\ &+ I\Big[A_1^{(j)}\Big(\Big(-\frac{2}{3}\sigma_1 + \frac{1\pi}{2}\sigma + 2\sigma_3\Big)\lambda_{1j}a_1 K_{\frac{1}{2}}(\lambda_{1j}a_1)\\ &+ \Big(-\frac{2}{3}\sigma_7 + \frac{1\pi}{2}\sigma + 2\sigma_5\Big)K_{\frac{3}{2}}(\lambda_{1j}a_1)\Big)\\ &+ B_1^{(j)}\Big(\Big(\frac{2}{3}\sigma_2 - \frac{\pi}{2}\sigma - 2\sigma_4\Big)\lambda_{2j}a_1 I_{\frac{1}{2}}(\lambda_{2j}a_1)\\ &+ \Big(-\frac{2}{3}\sigma_8 + \frac{\pi}{2}\sigma + 2\sigma_6\Big)I_{\frac{3}{2}}(\lambda_{2j}a_1)\Big)\Big],\end{aligned} \tag{5.11}$$

$$
\begin{aligned}
T_m = -2I\pi^2\mu a_1^{-\frac{1}{2}} \sum_{j=1}^{2} \Bigg[-A_1^{(j)} \Big((\xi^{-2} + \xi'^{-2}) \lambda_{1j} a_1 K_{\frac{1}{2}}(\lambda_{1j} a_1) \\
+ (\xi^{-2} \lambda_{1j}^2 a_1^2 + (\xi^{-2} + 3\xi'^{-2})) K_{\frac{3}{2}}(\lambda_{1j} a_1) \Big) \\
+ B_1^{(j)} \Big((\xi^{-2} + \xi'^{-2}) \lambda_{2j} a_1 I_{\frac{1}{2}}(\lambda_{2j} a_1) \\
- (\xi^{-2} \lambda_{2j}^2 a_1^2 + (\xi^{-2} + 3\xi'^{-2})) I_{\frac{3}{2}}(\lambda_{2j} a_1) \Big) \Bigg].
\end{aligned} \tag{5.12}
$$

6 Results and discussions

In order to satisfy the boundary condition over the entire semicircular arc of a sphere, it is necessary to resolve an infinite number of unknown constants. As a result of boundary collocation, the infinite series can be truncated into manageable finite representations by applying the boundary condition at a finite number of discrete points along the arc. It is possible to truncate the series after N terms by imposing a boundary condition at N discrete points, which leads to a system of $2N$ simultaneous linear equations. In order to clarify the unknown constants, the equations can be solved using a matrix reduction technique. By increasing N, the accuracy of this truncation can be improved, with the magnitude of the truncation error diminishing as N approaches infinity. This combination of methods provides a robust framework for analyzing the axisymmetric creeping flow generated by the particles in a couple stress fluid. For the application of boundary conditions in fluid dynamics, this method emphasizes the strategic selection of points along the semicircular arc of a sphere.

Overall, our initial point of selection is $\theta = \frac{\pi}{2}$, since this defines the area projected from the particle normal to the direction of motion. Furthermore, the points $\theta = 0$ and $\theta = \pi$ are also significant, although their use may lead to the formation of a singular coefficient matrix in the equations for the unknown constants A_n and B_n. There are four fundamental collocation points that are chosen to address this issue while maintaining symmetry: $\theta = \varepsilon$, $\theta = \frac{\pi}{2} - \varepsilon$, and $\theta = \pi - a$. The optimal value of ε is 0.01°, which allows the numerical results for drag force to converge to at least four significant figures. Using a sufficient number of well-distributed collocation points, the solution for the torque can be approximated accurately, regardless of the particle's actual form or boundary conditions in previous studies [28–30].

The consequences of these studies are then explored in detail, along with how the presence of couple stresses affect the fluid's behavior under different flow circumstances. When a fluid is able to withstand internal couple stresses, for example, its flow resistance changes, or it produces unique stress distributions compared with other fluids. In addition to discussing flow across porous media, it would also be interesting to discuss the impact of couple stress fluids on the microstructure of the porous matrix, which could alter permeability or other important parameters. The relevant parameters are the length of the first and second couple stress parameters, ξ and ξ', which take the range from 1.0 to ∞, the permeability parameter, α, which value from 1 to ≈10, the separation distance $\delta = (a_2 - a_1)/h = 1.001 \ldots 10$, the size ratio $a_1/a_2 = 0.1 \ldots 0.99$, and the angular speeds Ω_2/Ω_1. This work discussed the normalized torque with respect to stress tensor T_z/T_∞ and couple stress tensor T_m/T_∞ that appears graphically from Figures 2–11 and Table 1.

Figure 2 illustrates the normalized torque T_z/T_∞ as a function of the separation distance $(a_2 - a_1)/h$ for different values of the angular velocity ratio Ω_2/Ω_1. The data are presented for a fixed set of parameters: $\xi = 4.0$, $a_1 = 0.2$, $a_2 = 2.0$, and $\alpha = 1.5$. The curves show how normalized torque varies with separation distance for various angular velocity ratios, ranging from $\Omega_2/\Omega_1 = -4.0$ to other values. The torque remains relatively constant for most values of $(a_2 - a_1)/h$, suggesting a stable behavior in the system across different conditions. The variations in the curves indicate how changes in the angular velocity ratio influence the torque for the given configuration. This figure provides insights into the relationship between torque and separation distance, highlighting the impact of angular velocity ratios in the system dynamics.

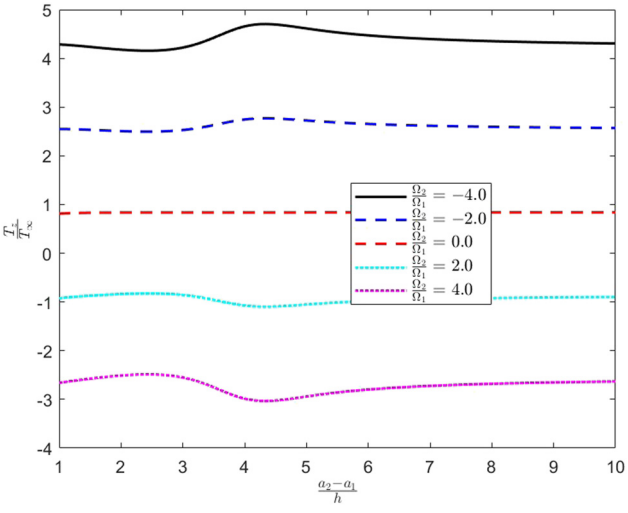

Figure 2: Normalized torque T_z/T_∞ *versus* the separation distance for various values of angular velocity ratio Ω_2/Ω_1 at $\xi = 4.0$, $a_1/a_2 = 0.2$, $\xi' = 2.0$, and $\alpha = 1.5$.

Table 1: Dimensionless torque T_z/T_∞ on the rigid sphere a_1 with $\xi = \xi' = 30$ and the two spheres rotating in opposite directions

$\frac{a_2-a_1}{h}$	a_1/a_2	α = 0.0 [9]	α = 1.0	α = 2.0	α = 3.0	α = 4.0	α = 10.0
1.05	0.1	2.122441	0.009290	0.013862	0.018227	0.021941	0.024624
	0.2	2.269303	0.014601	0.014031	0.018232	0.021941	0.024624
	0.3	2.430441	0.026206	0.016550	0.018576	0.021983	0.024624
	0.4	2.631674	0.038509	0.023930	0.021166	0.022742	0.024624
	0.5	2.910755	0.047317	0.034613	0.028292	0.026541	0.024649
	0.6	3.335021	0.066856	0.051530	0.041589	0.035944	0.025059
	0.7	4.056916	0.091365	0.074623	0.062736	0.054287	0.028426
	0.8	5.530868	0.141426	0.119717	0.103982	0.092054	0.044943
	0.9	10.023727	0.296392	0.259082	0.231912	0.210972	0.119431
	0.99	91.579170	3.090827	2.735826	2.466769	2.249198	1.119105
	0.999	907.585754	30.995344	27.398773	24.645763	22.394852	10.498260
4.0	0.1	2.010692	0.009295	0.013862	0.018227	0.021941	0.024624
	0.2	2.026726	0.015348	0.014058	0.018232	0.021941	0.024624
	0.3	2.069914	0.028412	0.016953	0.018630	0.021989	0.024624
	0.4	2.156706	0.040973	0.024844	0.021446	0.022817	0.024624
	0.5	2.312791	0.047696	0.034379	0.027981	0.026323	0.024646
	0.6	2.587229	0.066756	0.051112	0.041254	0.035741	0.025053
	0.7	3.093276	0.089896	0.073039	0.061348	0.053186	0.028289
	0.8	4.170103	0.137255	0.115798	0.100496	0.089002	0.043807
	0.9	7.512265	0.284453	0.248203	0.222316	0.202500	0.115038
	0.99	68.504509	2.943968	2.599263	2.342640	2.135705	1.033162
	0.999	678.908569	29.496065	25.994425	23.357748	21.205435	9.537851
10.0	0.1	2.010401	0.009307	0.013862	0.018227	0.021941	0.024624
	0.2	2.024912	0.015545	0.014066	0.018233	0.021941	0.024624
	0.3	2.065131	0.028598	0.016992	0.018636	0.021990	0.024624
	0.4	2.147774	0.041094	0.024896	0.021464	0.022822	0.024624
	0.5	2.298784	0.047732	0.034379	0.027976	0.026321	0.024646
	0.6	2.567110	0.066757	0.051095	0.041242	0.035736	0.025054
	0.7	3.065037	0.089818	0.072955	0.061275	0.053130	0.028285
	0.8	4.128208	0.137021	0.115577	0.100300	0.088830	0.043746
	0.9	7.433049	0.283770	0.247572	0.221747	0.201987	0.114743
	0.99	67.771484	2.935644	2.591443	2.335432	2.129021	1.027992
	0.999	671.643616	29.411222	25.914204	23.283249	21.135777	9.480927
∞	0.1	2.010351	0.009310	0.013862	0.018227	0.021941	0.024624
	0.2	2.024594	0.015580	0.014068	0.018233	0.021941	0.024624
	0.3	2.064278	0.028634	0.016999	0.018637	0.021990	0.024624
	0.4	2.146158	0.041117	0.024906	0.021467	0.022823	0.024624
	0.5	2.296226	0.047739	0.034379	0.027975	0.026321	0.024646
	0.6	2.563412	0.066757	0.051092	0.041240	0.035735	0.025054
	0.7	3.059825	0.089803	0.072939	0.061262	0.053120	0.028284
	0.8	4.120455	0.136976	0.115536	0.100263	0.088798	0.043734
	0.9	7.418374	0.283641	0.247452	0.221639	0.201890	0.114686
	0.99	67.635643	2.934221	2.590061	2.334135	2.127805	1.027024
	0.999	670.301086	29.415516	25.912762	23.278940	21.129986	9.472232

Figure 3 presents the normalized torque T_z/T_∞ as a function of the separation distance $(a_2 - a_1)/h$ for various values of the ratio a_1/a_2. The analysis is based on a fixed set of parameters: ξ = 10.0, Ω_2/Ω_1 = 10.0, and α = 1.0. The curves indicate that as the separation distance approaches zero, the normalized torque experiences a significant drop, particularly for lower values of a_1/a_2 (*e.g.*, 0.1). This behavior highlights the strong dependency of torque on the geometric configuration and the angular velocity ratio. The marked differences in the torque values suggest that the system dynamics are highly sensitive to the separation distance, with larger values of a_1/a_2 leading to more stable torque levels at increased distances.

Figure 4 depicts the normalized torque T_z/T_∞ as a function of the separation distance $(a_2 - a_1)/h$ for various values of the parameter ξ while holding a_1/a_2 = 0.4,

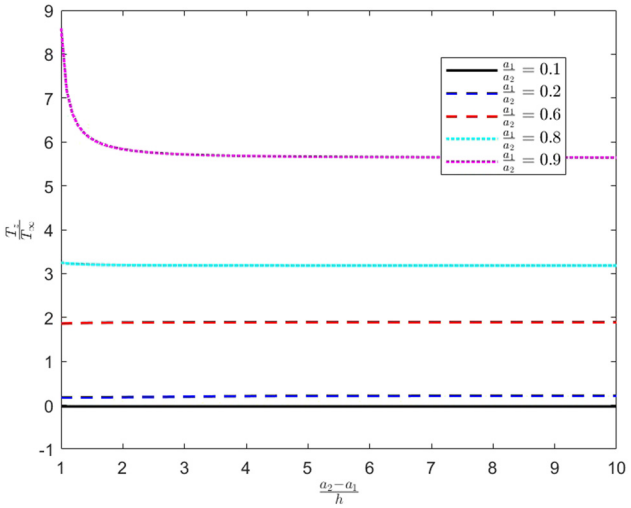

Figure 3: Normalized torque T_z/T_∞ *versus* the separation distance for various values of angular velocity ratio a_1/a_2 at $\xi = 10.0$, $\Omega_2/\Omega_1 = 10.0$, $\xi' \to \infty$, and $\alpha = 1.0$.

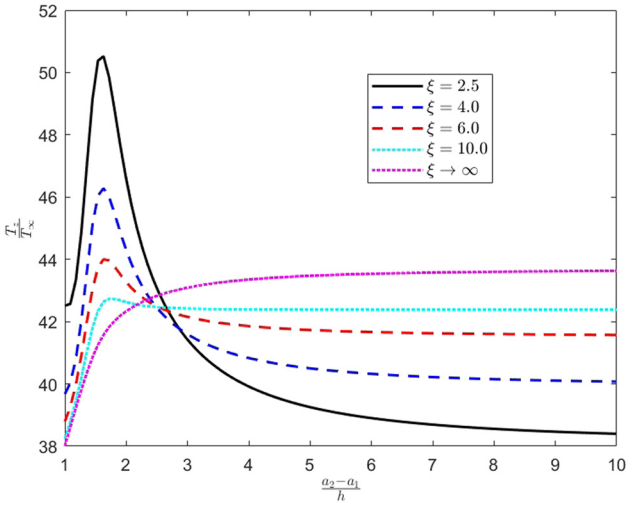

Figure 4: Normalized torque T_z/T_∞ *versus* the separation distance for various values of angular velocity ratio ξ at $a_1/a_2 = 0.4$, $\Omega_2/\Omega_1 = 4.0$, $\xi' = 1.0$, and $\alpha = 1.0$.

$\Omega_2/\Omega_1 = 4.0$, and $\alpha = 1.0$. The analysis reveals a pronounced sensitivity of the normalized torque to variations in the separation distance, particularly as it approaches zero. At lower values of ξ (*e.g.*, 2.5), the torque exhibits a dramatic increase, highlighting the enhanced coupling effects within the system under tighter spatial constraints. Conversely, higher values of ξ reflect a more gradual torque response, indicating a transition toward a more stable dynamical regime. This behavior can be attributed to the interplay between angular momentum transfer and the geometric configuration, which collectively dictate the system's

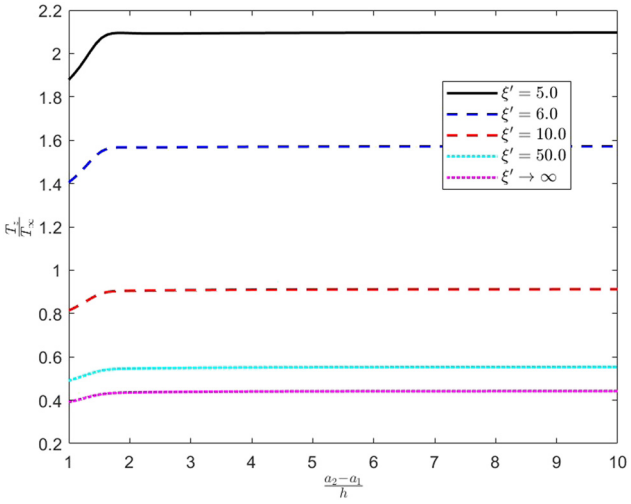

Figure 5: Normalized torque T_z/T_∞ *versus* the separation distance for various values of angular velocity ratio ξ' at $a_1/a_2 = 0.4$, $\Omega_2/\Omega_1 = 4.0$, $\xi = 10.0$, and $\alpha = 1.0$.

mechanical stability. The steep gradients observed in the curves illustrate the non-linear characteristics of torque as influenced by both the separation distance and the angular velocity ratio.

Figure 5 illustrates the normalized torque T_z/T_∞ as a function of the separation distance $(a_2 - a_1)/h$ for various values of the angular velocity ratio ξ', with parameters fixed at $a_1/a_2 = 0.4$, $\Omega_2/\Omega_1 = 4.0$, $\xi = 10.0$, and $\alpha = 1.0$. The data reveal a striking characteristic: as a_s/h increases, the normalized torque stabilizes at values near unity, irrespective of the specific value of ξ'. This observation underscores a significant decoupling of the torque from the separation distance for larger ξ', indicating that the system approaches a state of dynamic equilibrium. At lower values of ξ' (*e.g.*, 5.0), there is a more pronounced response to changes in separation, suggesting that the system remains sensitive to spatial configurations and angular momentum interactions. However, as ξ' increases, the curves converge, indicating a reduction in the influence of angular velocity on the torque dynamics. This behavior highlights the transition from a regime dominated by angular momentum transfer dynamics to one where the geometric factors play a more pivotal role. Overall, Figure 5 provides valuable insights into the torque characteristics of the system, illustrating how varying angular velocities can modulate the torque response over different spatial configurations, ultimately leading to a regime of stability at higher separations.

Figure 6 presents the normalized torque T_z/T_∞ as a function of the separation distance $(a_2 - a_1)/h$ for various values of the angular velocity ratio α, while maintaining $a_1/a_2 = 0.4$, $\Omega_2/\Omega_1 = 4.0$, and $\xi' = \infty$. The trends observed in this figure reveal critical insights into the torque behavior

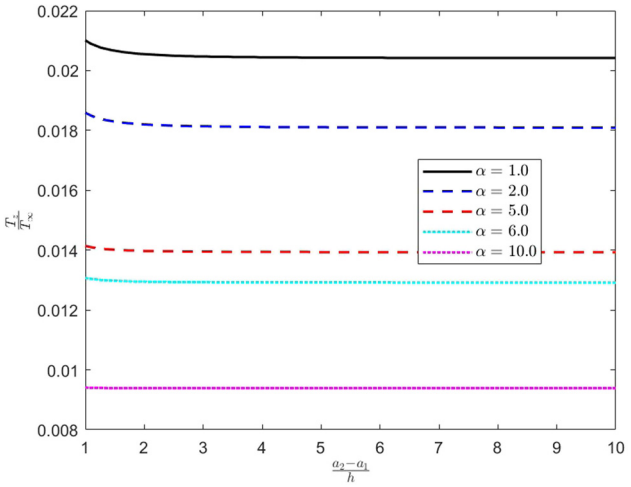

Figure 6: Normalized torque T_z/T_∞ *versus* the separation distance for various values of angular velocity ratio α at $a_1/a_2 = 0.9$, $\Omega_2/\Omega_1 = 4.0$, and $\xi' = \xi \to \infty$.

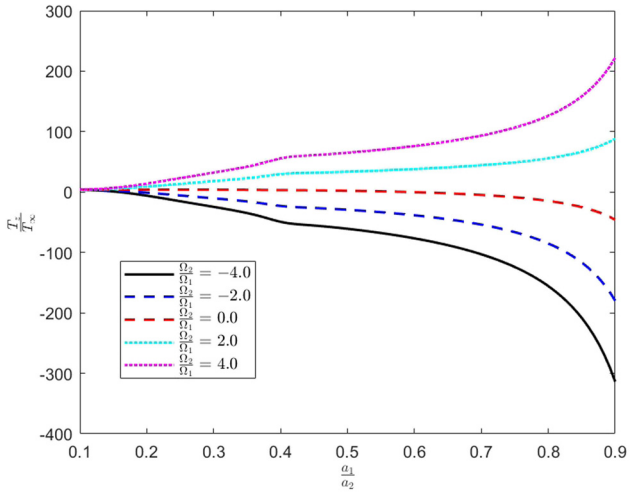

Figure 7: Normalized torque T_z/T_∞ *versus* the size ratio for various values of angular velocity ratio Ω_2/Ω_1 at $\frac{a_2-a_1}{h} = 1.5$, $\alpha = 1.0$, $\xi' = 1.0$, and $\xi = 4.0$.

as influenced by the angular velocity ratio. At lower values of α (*e.g.*, 1.0), the normalized torque exhibits a relatively steep rise with decreasing separation distance, indicating a robust coupling between the components of the system. This behavior suggests that as the components come closer, the interactions become increasingly significant, leading to enhanced torque generation. The underlying physics can be attributed to the increased angular momentum transfer and the proximity-induced coupling effects, which dominate the torque dynamics in this regime. As α increases, particularly beyond 2.0, a noticeable shift in the torque response is observed. The curves begin to flatten out, suggesting that the system approaches a more stable regime where the torque becomes less sensitive to changes in separation distance.

This indicates that higher angular velocities contribute to a more uniform distribution of forces within the system, thereby reducing the torque fluctuations as the separation varies. For larger values of α (*e.g.*, 10.0), the normalized torque approaches a near-constant value across a wide range of separation distances. This behavior highlights a significant decoupling of torque from spatial configurations, suggesting that the dynamics are increasingly governed by the balance of forces rather than the geometric arrangement of the components. Overall, Figure 6 illustrates how the angular velocity ratio significantly influences the torque response in the system. The transition from a sensitivity to separation distance at lower α values to a stable, nearly constant torque at higher α values emphasizes the complex interplay between angular momentum dynamics and geometric configurations, ultimately shedding light on the stability characteristics of the system under varying operational conditions.

Figure 7 illustrates the normalized torque T_1/T_∞ as a function of the size ratio ξ_1/ξ_2 for various values of the angular velocity ratio Ω_2/Ω_1, with other parameters fixed: $\alpha = 1.5$, $\xi' = 1.0$, and $\xi = 4.0$. The graph clearly demonstrates how the normalized torque behaves under different conditions of size and velocity ratios. As the size ratio increases, the torque initially shows a positive trend for certain angular velocity ratios, particularly for the higher values of Ω_2/Ω_1 (represented by the magenta and cyan curves). In contrast, for lower velocity ratios (shown by the black and blue curves), the normalized torque decreases and eventually becomes negative. The trend indicates a significant influence of the angular velocity ratio on the torque's direction and magnitude, highlighting how the relative sizes of the objects and their rotational velocities impact the overall system dynamics.

Figure 8 presents the normalized torque T_m/T_∞ as a function of the size ratio ξ_1/ξ_2 for various values of permeability parameter α, while keeping the other parameters constant: $\xi = 10.0$, $\xi' = 20.0$, and $\Omega_2/\Omega_1 = -2.0$. The graph shows a clear increase in normalized torque with the increasing size ratio, and this effect becomes more pronounced as the permeability parameter α increases. For smaller values of α (represented by the black and blue curves), the torque increases gradually with the size ratio, but the slope remains relatively mild. As α increases, particularly for $\alpha = 4.0$ and $\alpha = 5.0$ (indicated by the pink and green curves), the torque increases at a much sharper rate. This suggests that higher permeability values significantly amplify the effect of the size ratio on the normalized torque, leading to a much steeper rise in torque. This behavior is important for systems where permeability plays a key role, such as in porous materials or fluid–structure

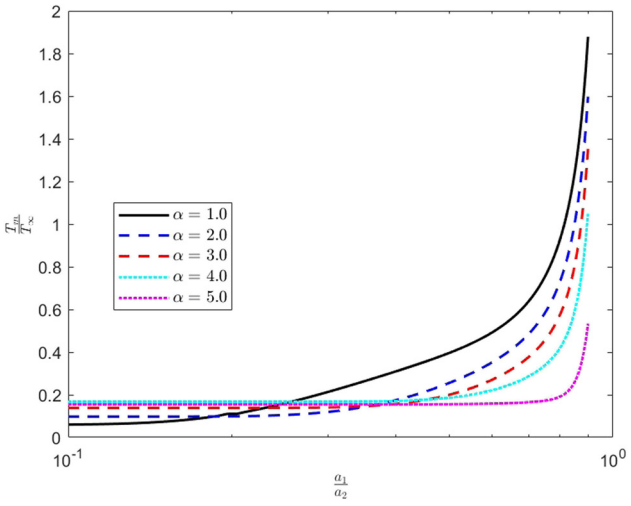

Figure 8: Normalized torque T_m/T_∞ *versus* the size ratio for various values of permeability α at $\frac{a_2-a_1}{h}$ = 10.0, Ω_2/Ω_1 = –2.0, ξ' = 10.0, and ξ = 20.0.

interaction problems, where changes in permeability can have a substantial impact on the overall mechanical or fluid dynamic performance.

Figure 9 illustrates the normalized torque T_m/T_∞ as a function of the size ratio ξ_1/ξ_2 for various values of angular velocity ratio Ω_2/Ω_1, while keeping other parameters fixed: α = 1.0, ξ' = 1.0, and ξ = 4.0. The results show that the torque behavior is strongly influenced by the angular velocity ratio. For negative values of Ω_2/Ω_1, represented by the curves for Ω_2/Ω_1 = −4.0 (black) and Ω_2/Ω_1 = −2.0 (blue), the normalized torque decreases initially as the size ratio increases and eventually rises steeply for larger size ratios. The other curves, representing lower angular velocity ratios (*e.g.*, Ω_2/Ω_1 = 0.0, Ω_2/Ω_1 = 2.0, and Ω_2/Ω_1 = 4.0), exhibit a more gradual increase in torque with the size ratio. The trends indicate that for negative angular velocity ratios, the torque tends to decrease initially before increasing, whereas for positive angular velocity ratios, the torque steadily increases with the size ratio. This behavior underscores the significant role of angular velocity differences in controlling the torque generated in such systems, particularly in configurations where the angular velocities of the two objects differ.

Figure 10 illustrates the normalized torque T_m/T_0 as a function of the size ratio for different values of the length of the first couple stress parameter ξ. The graph plot values for ξ = 2.5, 4.0, 6.0, and 8.0 using various line styles. The curves demonstrate how the normalized torque behaves as the size ratio approaches 0.9, revealing distinct trends based on the chosen parameter values. Notably, as ξ increases, the torque approaches a limiting value, indicating a convergence in behavior among the different parameter settings.

Figure 11 displays the normalized torque T_m/T_0 as a function of the size ratio $\frac{\Omega_2}{\Omega_1}$ for various values of the second couple stress parameter ξ'. The plotted lines correspond to different parameter settings: ξ' = 2.5, 4.0, 6.0, 8.0, and 10.0. Notably, as the size ratio increases, the normalized torque exhibits an upward trend, indicating that larger size ratios lead to higher torque values. The divergence in the curves suggests that the choice of the second couple stress parameter significantly influences the relationship between torque and size ratio. As ξ' increases, the torque response becomes more pronounced, particularly at larger size ratios. This behavior highlights the importance of couple

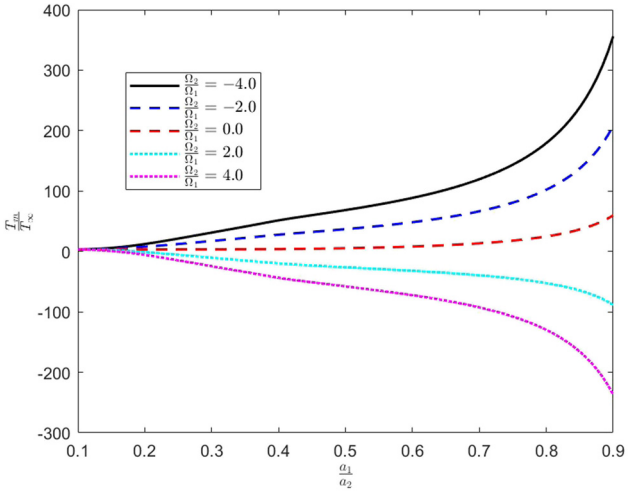

Figure 9: Normalized torque T_m/T_∞ *versus* the size ratio for various values of angular velocity ratio Ω_2/Ω_1 at $\frac{a_2-a_1}{h}$ = 1.5, α = 1.0, ξ' = 1.0, and ξ = 4.0.

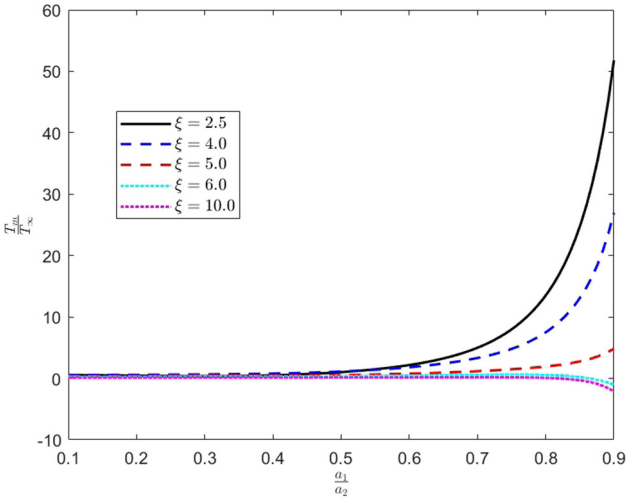

Figure 10: Normalized torque T_m/T_∞ *versus* the size ratio for various values of the length of the first couple stress parameter ξ at $\frac{a_2-a_1}{h} \to \infty$, α = 1.0, $\xi' \to \infty$, Ω_2/Ω_1 = –1.0.

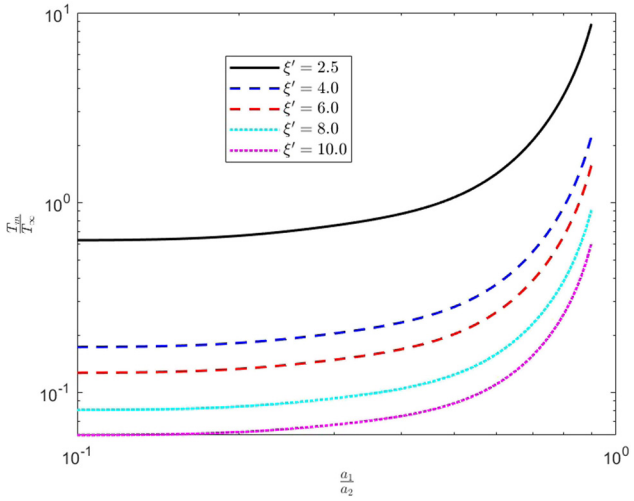

Figure 11: Normalized torque T_m/T_∞ *versus* the size ratio for various values of the length of the second couple stress parameter ξ' at $\frac{a_2-a_1}{h} = 3.0$, $\alpha = 1.0$, $\xi = 20$, $\Omega_2/\Omega_1 = -0.1$.

stress effects in analyzing torque in systems with varying geometrical configurations.

Our discussions can be summarized as the following main points:

- The variation of normalized torque with the separation distance and the size ratio between spheres for different angular velocity ratios shows that the decreasing torque trend at higher angular velocity ratios underscores the reduced influence of couple stress effects at elevated speeds, which is critical for dynamic system applications.
- The normalized torque as a function of parameters such as couple stress properties, size ratios, and permeability indicates that increasing couple stress parameters or adjusting size ratios significantly influences torque, offering pathways to optimize fluid behavior in engineering systems. The larger size ratios can enhance torque generation in systems with positive angular velocity ratios.
- This diagram illustrates how torque affects with couple stress parameter within the fluid medium. For small separation distances, it arrives at the maximum value, and at a certain point, it is near to $(a_2 - a_1)/h \approx 3$, reversing its direction to reach its minimum value. This aids in the development of predictive models and improving fluid–structure interaction analysis.
- For negative angular velocity ratios, the torque initially decreases before increasing, indicating a complex relationship influenced by the size ratio. But, for positive angular velocity ratios, the torque consistently increases with the size ratio, highlighting the direct impact of angular velocity differences on torque generation.
- As the first couple stress parameter (ξ) increases, the torque values stabilize, suggesting that higher couple stress characteristics lead to more consistent torque responses across varying size ratios.
- The normalized torque from couple stress increases with the size ratio $\frac{\Omega_2}{\Omega_1}$, indicating a stronger torque response at larger size ratios. This behavior is influenced by the second couple stress parameter ξ', with higher values leading to more pronounced torque variations.

7 Conclusions

The study investigates the torque acting on a solid sphere positioned within a spherical container filled with a porous medium saturated by incompressible couple stress fluids. It is hypothesized that the inner sphere moves along the axis of symmetry. A semi-analytical method is employed to derive the field functions and compute the torque associated with both stress and couple stress forces, with graphical representations provided. Additionally, numerical calculations of the torque, including limit cases, are presented in tabular form. The study of couple stress fluids in porous media has important applications. Furthermore, the future directions of this work could include (a) investigating the effects of varying permeability and fluid properties on stress distribution and flow behavior in couple stress media under different rotational speeds, (b) exploring the impact of eccentricity on stability and dynamic response in rotating systems, potentially incorporating non-linear fluid dynamics, and (c) developing predictive models that integrate experimental data to enhance the understanding of fluid–structure interactions in such media, informing applications in engineering and materials science. Also, the studies by Kumar and Jangili [31] and Siva *et al.* [32] delve into the complexities of electroosmotic flow in couple stress fluids within microchannels. While the former emphasizes heat transfer analysis in rotating systems, the latter investigates the impact of electromagnetohydrodynamics and slip-dependent zeta potentials on rotational flow dynamics. Together, they enhance the understanding of fluid behavior in microfluidic systems under coupled physical and thermal effects. On the other side [33–35], these studies explore various effects on magnetohydrodynamic flows, focusing on the Soret, Joule, and Hall effects in rotating mixed convective scenarios. They investigated the behavior of elastico-viscous fluids through porous media and the implications of ion slip in unsteady conditions. These studies contribute to a deeper understanding of fluid

dynamics in engineering applications involving magnetic fields. These can be taken into account in the future work.

Acknowledgments: This study was supported by Princess Nourah bint Abdulrahman University Researchers Supporting Project Number (PNURSP2024R215), Princess Nourah bint Abdulrahman University, Riyadh, Saudi Arabia.

Funding information: This study was supported by Princess Nourah bint Abdulrahman University Researchers Supporting Project Number (PNURSP2024R215), Princess Nourah bint Abdulrahman University, Riyadh, Saudi Arabia.

Author contributions: All authors were involved in the overall planning and design of the study. Shreen El-Sapa was responsible for writing, collecting data, and analyzing the results. Dr. Amal Al-Hanaya wrote the initial draft of the manuscript, which was then reviewed and improved upon by all authors. All authors have accepted responsibility for the entire content of this manuscript and approved its submission.

Conflict of interest: The authors state no conflict of interest.

Data availability statement: All data generated or analysed during this study are included in this published article.

References

[1] Deo S, Gupta BR. Drag on a porous sphere embedded in another porous medium. J Porous Media. 2010;13(11):1009–16. doi: 10.1615/JPorMedia.v13.i11.70.

[2] Leontev NE. Flow past a cylinder and a sphere in a porous medium within the framework of the Brinkman equation with the Navier boundary condition. Fluid Dynam. 2014;49(2):232–7. doi: 10.1134/S0015462814020112.

[3] El-Sapa S. Effect of permeability of Brinkman flow on thermophoresis of a particle in a spherical cavity. Europ J Mech-B/Fluids. 2020;79:315–23. doi: 10.1016/j.euromechflu.2019.09.017.

[4] Faltas MS, Sherief HH, Allam AA, Ahmed BA. Mobilities of a spherical particle straddling the interface of a semi-infinite Brinkman flow. J Fluids Eng. 2021;143(7):071402. doi: 10.1115/1.4049931.

[5] Madasu KP, Bucha T. Influence of MHD on micropolar fluid flow past a sphere implanted in porous media. Indian J Phys. 2021;95(6):1175–83. doi: 10.1007/s12648-020-01759-7.

[6] Stokes VK. Couple stresses in fluids. In: Theories of fluids with microstructure: an introduction. Springer; 1984. p. 34–80.

[7] Stokes VK. Theories of fluids with microstructure: an introduction. Berlin, Germany: Springer Science and Business Media; 2012.

[8] Jangili S, Adesanya SO, Ogunseye HA, Lebelo R. Couple stress fluid flow with variable properties: a second law analysis. Math Meth Appl Sci. 2019;42(1):85–98.

[9] Al-Hanaya A, El-Sapa S, Ashmawy EA. Axisymmetric motion of an incompressible couple stress fluid between two eccentric rotating spheres. J Appl Mech Tech Phys. 2022;63(5):1–9.

[10] El-Sapa S, Almoneef A. Axisymmetric migration of an aerosol particle embedded in a Brinkman medium of a couple stress fluid with slip regime. Europ J Pure Appl Math. 2022;15(4):1566–92.

[11] Majumdar SR. On the slow motion of viscous liquid in space between two eccentric spheres. J Phys Soc Japan. 1969;26(3):827–40.

[12] Kamel MT, Saint John NB, Chan Man Fong CF. Micropolar fluid flow between two eccentric coaxially rotating spheres. Acta Mech. 1993;99:155–71.

[13] Munson BR. Viscous incompressible flow between eccentric coaxially rotating spheres. Phys Fluids. 1974;17(3):528. doi: 10.1063/1.1694750.

[14] Sherief HH, Faltas MS, El-Sapa S. A general formula for the drag on a solid of revolution body at low Reynolds numbers in a micro-stretch fluid. Meccanica. 2017;52(11–12):2655–64.

[15] El-Sapa S. Interaction between a non-concentric rigid sphere immersed in a micropolar fluid and a spherical envelope with slip regime. J Mol Liquids. 2022;351:118611.

[16] Davis AMJ. Force and torque on a rotating sphere close to and within a fluid-filled rotating sphere. In: Proceedings of the 59th Annual Meeting of the APS Division of Fluid Dynamics. American Physical Society; November 2006.

[17] Madasu KP, Sarkar P. Torque on the slow rotation of a slightly deformed slip sphere in a Brinkman medium. Pramana. 2023;97(1):44.

[18] Maike S, Schröder J, Bluhm J, Ricken T. A mesh-in-element method for the theory of porous media. Z Angew Math Mech. 2024;64. doi: 10.1002/nme.7565.

[19] El-Sapa S, Al-Hanaya A. Effects of slippage and permeability of couple stress fluid squeezed between two concentric rotating spheres. Phys Fluids. 2023;35:103112.

[20] Yadav PK, Roshan M. Mathematical modeling of blood flow in an annulus porous region between two coaxial deformable tubes: An advancement to peristaltic endoscope. Chin J Phys. 2024;88:89–109.

[21] Yadav PK, Roshan M. Mathematical modeling of creeping electromagnetohydrodynamic peristaltic propulsion in an annular gap between sinusoidally deforming permeable and impermeable curved tubes. Phys Fluids. 2024;36(7):071907. doi: 10.1063/5.0217370.

[22] Sharma R, Thakur K. On couple-stress fluid heated from below in porous medium in hydromagnetics. Czechoslovak J Phys. 2000;50:753–8.

[23] Chand R, Rana G, Yadav D. Thermal instability in a layer of couple stress nanofluid saturated porous medium. J Theoretic Appl Mech. 2017;47:69.

[24] Ochoa-Tapia JA, Whitaker S. Momentum transfer at the boundary between a porous medium and a homogeneous fluid- II. Comparison with experiment. Int J Heat Mass Transfer. 1995;38(14):2647–55.

[25] Ochoa-Tapia JA, Whitaker S. Momentum transfer at the boundary between a porous medium and a homogeneous fluid-I. Theoretical development. Int J Heat Mass Transfer. 1995;38(14):2635–46.

[26] Madasu KP, Sarkar P. Couple stress fluid past a sphere embedded in a porous medium. Archive Mech Eng. 2022;5–19.

[27] Ramkissoon H. On the rotation of an axially symmetric body in couple stress fluids. Z Angew Math Mech. 1984;64:297–302.

[28] Faltas MS, Nashwan MG, Ahmed BA, Hamdy P. Oscillations of a spherical particle in the presence of a flat interface separating two fluid phases. Chinese J Phys. 2024;89:1377–99.
[29] Faltas MS, Sherief HH, El-Maghraby NM, Wanas EF. The electrokinetic flow of a micropolar fluid in a microtube with velocity and spin velocity slippage. Chinese J Phys. 2024;89:504–27.
[30] Faltas MS, Ashmawy EA, Sherief HH, Othman HA. Oscillations of coaxial hydrophobic spherical colloidal particles in a micropolar fluid. Phys Fluids. 2024;36(5):052017.
[31] Kumar B, Jangili S. Heat transfer analysis of electroosmotic flow of couple stress fluid through a rotating circular microchannel. Int J Thermal Sci. February 2025;208:109359.
[32] Siva T, Dubey D, Jangili S. Rotational flow dynamics of electroosmotic transport of couple stress fluid in a microfluidic channel under electromagnetohydrodynamic and slip-dependent zeta potential effects. Phys Fluids. 2024;36(9):092006. doi: 10.1063/5.0215302.
[33] Veera Krishna M, Swarnalathamma BV, Chamkha AJ. Investigations of Soret. Joule and Hall effects on MHD rotating mixed convective flow past an infinite vertical porous plate. J Ocean Eng Sci. 2019;4(3):263–75.
[34] Veera Krishna M, Chamkha AJ. Hall and ion slip effects on MHD rotating flow of elastico-viscous fluid through porous medium. Int Commun Heat Mass Transfer. 2020;113:104494.
[35] Veera Krishna M, Ameer Ahamad N, Chamkha AJ. Hall and ion slip effects on unsteady MHD free convective rotating flow through a saturated porous medium over an exponential accelerated plate. Alexandr Eng J. 2020;59(2):565–77.